Supporting Information for

Tuning the Charge Distribution of Co-N-C Active Sites for Enhanced Trifunctional Electrocatalysis

Zhaopeng Sun,[†,☆] Yaling Wu,[†,☆] Yingying Chen,[†] Zhibo Li,[†] Sen Lei,[†,‡] Yongyong Cao,[*,†] Lianwen Zhu,[†] Xuebo Cao,[*,†] and Zheng Yan[*,†]

[†] College of Biological, Chemical Sciences and Engineering, Jiaxing University, Jiaxing 314001, P. R. China

[‡] School of Chemistry and Chemical Engineering, Zhejiang Sci-Tech University, Hangzhou 310018, China

☆ These authors contributed equally

* Correspondence to: yzheng158@zjxu.edu.cn (Z. Yan); cyy@zjxu.edu.cn (Y.-Y. Cao); xbcao@zjxu.edu.cn (X. Cao)

The table of Content **Page number**

Material characterization instruments. Powder X-ray diffraction (PXRD) was employed to examine the structure of the samples, utilizing a Shimadzu XRD-7000 diffractometer (Cu Kα radiation, λ=1.54056 Å) manufactured in Japan. Raman spectra were collected using a DXR2xi Raman imaging microscope (Thermo Fisher Scientific). Fourier transform infrared (FT-IR) spectral data were obtained using a Nicolet iS50 FT-IR produced by Thermo Fisher Scientific. A K-Alpha high-performance X-ray photoelectron spectroscopy (XPS) spectrometer produced by Thermo Fisher Scientific was utilized to conduct XPS analysis. Thermogravimetric analysis combined with differential scanning calorimetry (TG-DSC) was performed using a simultaneous thermal analyzer (SDT 650, TA Instruments/STA449F3, NETZSCH). Morphological characterization was conducted using a ZEISS Sigma 300 scanning electron microscope (SEM). Transmission electron microscopy (TEM) and energy-dispersive spectroscopy (EDS) analyses were performed on an FEI Tecnai G2 F20 electron microscope operated at 80 kV.

Electrochemical measurements. The electrocatalytic performance of all samples for ORR, OER, and HER was evaluated using a standard three-electrode setup with a CHI-760E electrochemical workstation (Chenhua, Shanghai). Among these electrodes, the working electrode is either a glassy carbon electrode (GC) or a rotating disk electrode (RRDE), while the counter electrode is a graphite rod. The choice of the reference electrode depends on the properties and concentration of the electrolyte solution. Specifically, in acidic and neutral media, as well as in a 0.1 M KOH alkaline solution, an Ag/AgCl (saturated KCl solution) electrode is used. In contrast, a 1.0 M KOH electrolyte system requires an Hg/HgO reference electrode. Preparation of the electrocatalyst ink: Mix 2.5 mg of the carbonized sample with 2.5 mg of carbon powder and grind the mixture thoroughly. The blended materials were then evenly dispersed in a mixture of 360 μL distilled water, 120 μL isopropanol, and 20 μL Nafion solution, followed by sonication for 60 minutes to yield a uniform ink. 4 μL and 8 μL of electrocatalyst ink were drop-cast onto the pre-polished GC (0.07069 cm^2) and RRDE (0.196 cm^2) electrodes, respectively, and air-dried to serve as working electrodes. 0.5 M H_2SO_4 (acidic), 0.1 M K_2SO_4 (neutral), 0.1 M KOH and 1.0 M KOH (alkaline) were used as the electrolyte solutions for ORR/OER/HER, with a scan rate of 5 mV s^{-1}. However, during the constant voltage test, 60 μL of the ink was evenly coated onto a 1 cm^2 carbon paper, serving as the working electrode. All potentials were converted to the reversible hydrogen electrode (RHE) scale using Equations S1 and S2.

Calculations

All potentials were corrected to the reversible hydrogen electrode (RHE), calculated by the Nernst equation:

$$E\ (V\ vs.\ RHE) = E\ (V\ vs.\ Ag/AgCl) + 0.197\ V + 0.0591 \times pH \quad \textbf{(Equation S1)}$$

$$E\ (V\ vs.\ RHE) = E\ (V\ vs.\ Hg/HgO) + 0.098\ V + 0.0591 \times pH \quad \textbf{(Equation S2)}$$

The Tafel slope was calculated by using the following equation S3.

$$\eta = b\log j + a \quad \textbf{(Equation S3)}$$

where η is the overpotential (V), j is the current density (mA cm^{-2}), and b is the Tafel slope (mV dec^{-1}).

The ORR mechanism based on electron transfer number was analyzed by using K-L equations：

$$\frac{1}{J} = \frac{1}{J_L} + \frac{1}{J_K} = \frac{1}{B\omega^{1/2}} \quad \textbf{(Equation S4)}$$

$$B = 0.2nFC_0D_0^{2/3}\upsilon^{-1/6} \quad \textbf{(Equation S5)}$$

where J is the measured current density (mA cm^{-2}); J_K is the kinetic current density (mA cm^{-2}); J_L is the diffusion limit current density (mA cm^{-2}); ω is the rotation speed of the rotating disc (rpm min^{-1}); F is the Faraday's constant (96485 C mol^{-1}); C_0 is the oxygen concentration in 0.1 M KOH solution (1.2×10^{-6} mol cm^{-1}); D_0 is the diffusion coefficient of oxygen in 0.1 M KOH solution (1.9×10^{-5} cm^2 s^{-1}); υ is the viscosity of 0.1 M KOH solution (1.13×10^{-5} cm^2 s^{-1}).

For RRDE measurements, set the Pt loop potential to 1.2 V and the H_2O_2 yield and electrons can be calculated. The formula for the number of electron-transfers (n) in the electrode reaction is as follows:

$$H_2O_2\% = 200 \times \frac{I_r/N}{I_d + I_r/N} \quad \textbf{(Equation S6)}$$

$$n = 4 \times \frac{I_d}{I_d + I_r/N} \quad \textbf{(Equation S7)}$$

Among them, I_d is the diffusion-current (A), I_r is the ring-current (A), and N is the collection efficiency of the platinum ring (with a value of 0.37).[1]

The electrochemically active surface area of samples was quantified by integrating the charge of the redox peaks at 1.18 V versus the reversible hydrogen electrode scale (vs. RHE) measured using cyclic voltammetry (CV) in 0.1and 1.0 M KOH.

$$Q = I \times t = I \times \frac{V - V_0}{v} = I \times \Delta U / v \qquad \textbf{(Equation S8)}$$

Where Q (C) refer to electric charge, I (A) as constant current, ΔU (V) refers to voltage window, and v (V s^{-1}) refers to scan rates (pay attention to unit conversion).

The electrochemically active surface area (ECSA) are usually estimated from the electrochemical double-layer capacitance (Cdl) via collecting cyclic voltammogram (CV). The Cdl was determined from cyclic voltammograms measured in a non-Faradaic region at different scan rates in the potential range from 0 to 0.1 V versus Ag/AgCl. The current differences at 0.1 V (with scan rates v = 20, 40, 60, 80 and 100 mV/s) were fitted to obtain the Cdl: Cdl = Ic/v, where Cdl, Ic, and v are the double-layer capacitance (mF/cm2) of the electroactive materials, charging current (mA/cm2), and scan rate (mV/s).[2-4]

All density functional theory (DFT) calculations were carried out with the Vienna Ab initio Simulation Package code.[5] The electron–ion interactions were treated using the projector augmented wave (PAW) method, while exchange–correlation effects were described by the Perdew–Burke–Ernzerhof (PBE) functional within the generalized gradient approximation (GGA).[6-8] A plane-wave cutoff energy of 520 eV was chosen, and structural relaxations were performed until the total energy and atomic forces converged within 1×10^{-5} eV and 0.05 eV $Å^{-1}$, respectively. To account for long-range dispersion forces, Grimme's DFT-D3 correction was included throughout.[9] The Brillouin zone was sampled using a 4 × 4 × 1 Monkhorst–Pack k-point grid for all structural optimized calculations.[10] A vacuum spacing larger than 15.0 Å was introduced along the z direction to eliminate spurious interactions between periodic slabs.

The Gibbs free energy profile for hydrogen evolution reaction (HER), oxygen reduction reaction (ORR) and oxygen evolution reaction (OER) were evaluated within the computational hydrogen electrode (CHE) framework proposed by Nørskov and co-workers under standard conditions.[11] The entropy of $H^+ + e^-$ pair is approximately regarded as half of H_2 entropy in standard condition. The free energy change for each elementary step was calculated using:

$$\Delta G = \Delta E + \Delta E_{ZPE} + \int \mathrm{CpdT} - \mathrm{T}\Delta S + \Delta G_U,$$

where ΔE represents the electronic energy obtained from DFT, ΔE_{ZPE} and ΔS correspond to zero-point energy and entropy contributions, $\int$CpdT denotes the enthalpic correction at 298.15 K, and ΔG_U = eU accounts for the electrode potential. The ultimate potential (U_L) characterizing catalytic activity is governed by the potential-determining step (PDS) in the most favorable pathway, and is quantified by the largest positive free-energy change (ΔG_{max}) of the optimal electrocatalysts ($-\Delta G_{max}$/e).

Carbon vacancies were introduced to maintain charge neutrality and structural stability of the Co^{3+} coordination environment, rather than to intentionally create additional active sites. To examine whether carbon vacancies could serve as potential reaction centers, we explicitly evaluated O_2 adsorption at the carbon vacancy sites. As shown in Fig S15, O_2 does not adsorb on the carbon vacancy sites and remains far from the catalyst surface, with a much weaker adsorption energy (0.41 eV) compared to that on the Co metal centers (−0.63 eV). These results indicate that carbon vacancies do not provide energetically favorable or catalytically relevant adsorption sites, and the catalytic activity is therefore dominated by the Co-centered active sites.

In addition, we systematically examined the side-on and end-on adsorption configurations of O_2 on the metal sites. As shown in Fig S16, geometry optimizations reveal that on the Co^{2+}–N–C site, the end-on configuration of O_2 is energetically more favorable (−0.73 eV) than the side-on configuration (−0.31 eV). In contrast, for the Co^{3+}–N–C site, O_2 initially placed in either side-on or end-on configurations converges to an end-on geometry after optimization, with an adsorption energy of −0.63 eV. Consequently, the end-on adsorption mode was adopted for all subsequent free-energy calculations.

We have performed additional electronic structure analyses, including partial density of states (PDOS) calculations (Fig S17), to further elucidate the origin of the different adsorption behaviors between Co^{2+} and Co^{3+} sites. Compared with Co^{3+}–N–C, the Co^{2+}–N–C site exhibits a higher contribution of occupied Co 3d states extending toward the Fermi level, as revealed by the PDOS. Owing to its $3d^7$ configuration, Co^{2+} retains partially filled d orbitals whose occupied states lie closer to Fermi level, whereas the higher-valence Co^{3+} shows a deeper-lying occupied manifold and reduced PDOS near Fermi level. This upward shift of occupied Co 3d states in Co^{2+} enhances their energetic alignment with the frontier orbitals of oxygenated intermediates and H*, enabling more efficient electron donation during adsorption. At the same time, the absence of excessive unoccupied

d states near Fermi level avoids overly strong d–p hybridization, resulting in a balanced adsorption strength for *O, *OH, OOH, and H.

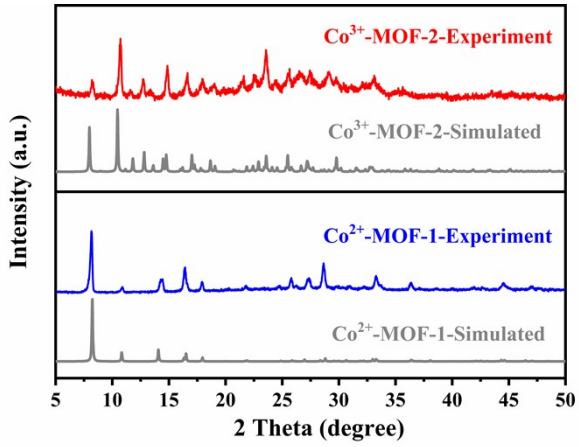

Figure S1. PXRD patterns of Co−MOFs centered around two different valence states of cobalt.

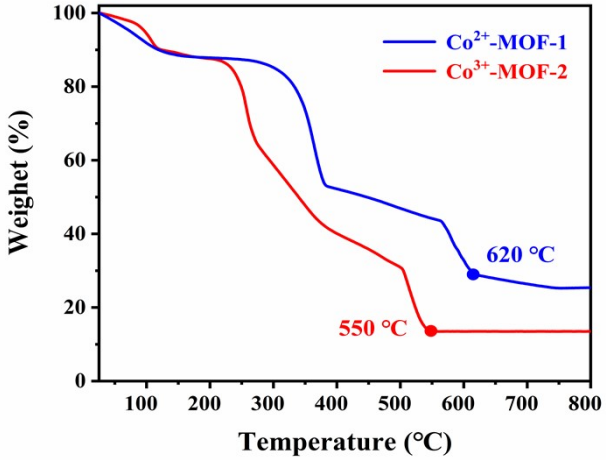

Figure S2. TG curves of Co−MOFs with two different valence state centers.

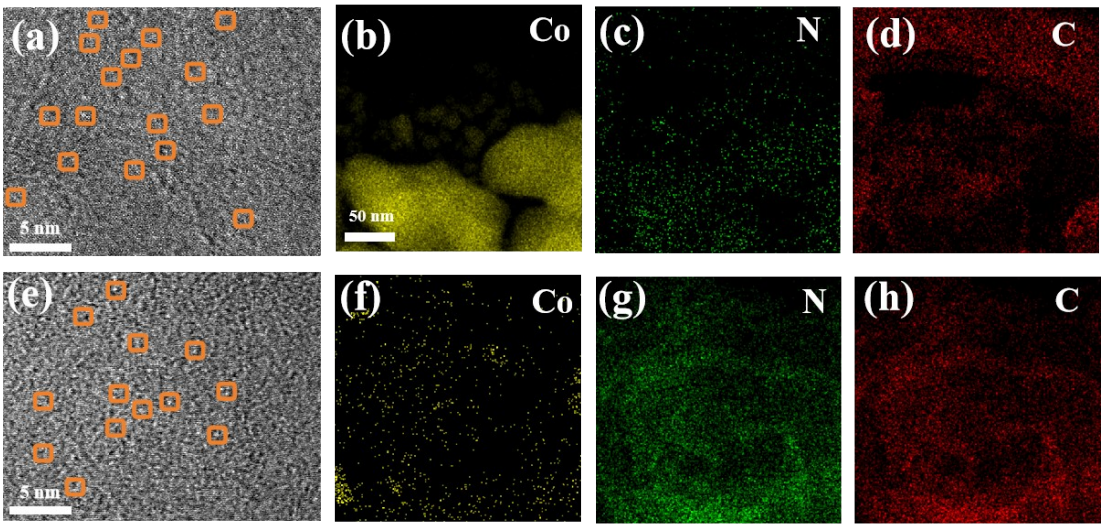

Figure S3. (a-d) STEM and mapping images of **Co^{2+}–N–C** at different sizes; (e-h) STEM and mapping images of **Co^{3+}–N–C**.

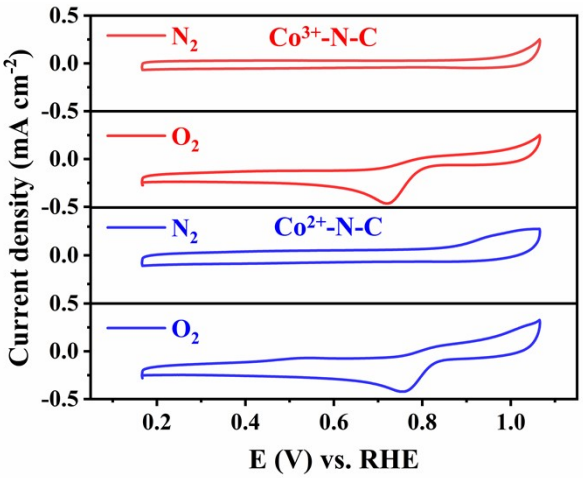

Figure S4. CV plots of **Co–N–C** catalysts with two different metal valence-centered states in 0.1 M KOH electrolyte, under N_2 and O_2 saturated conditions.

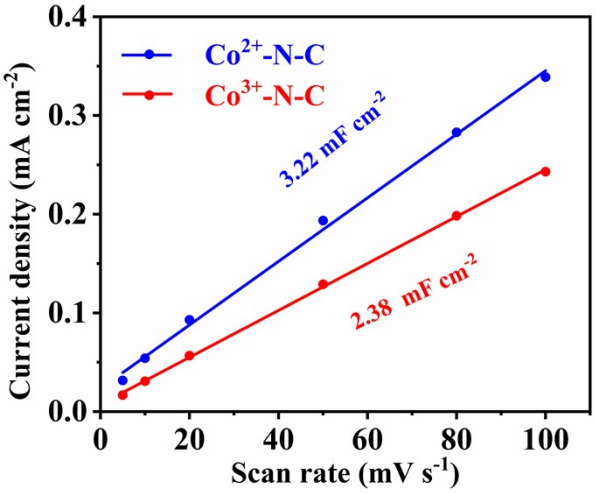

Figure S5. Electric double-layer capacitance (C_{dl}) diagrams of **Co−N−C** in a 0.1 M KOH electrolyte.

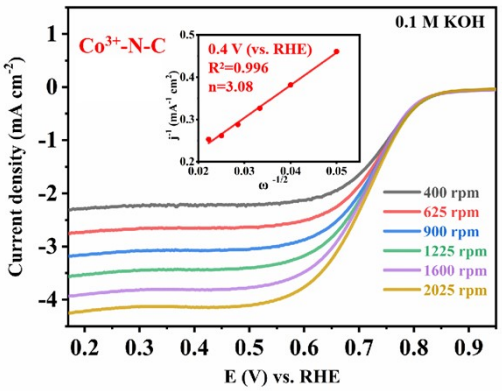

Figure S6. LSV curves and K-L illustrations of **Co^{3+}−N−C** at 400−2025 rpm.

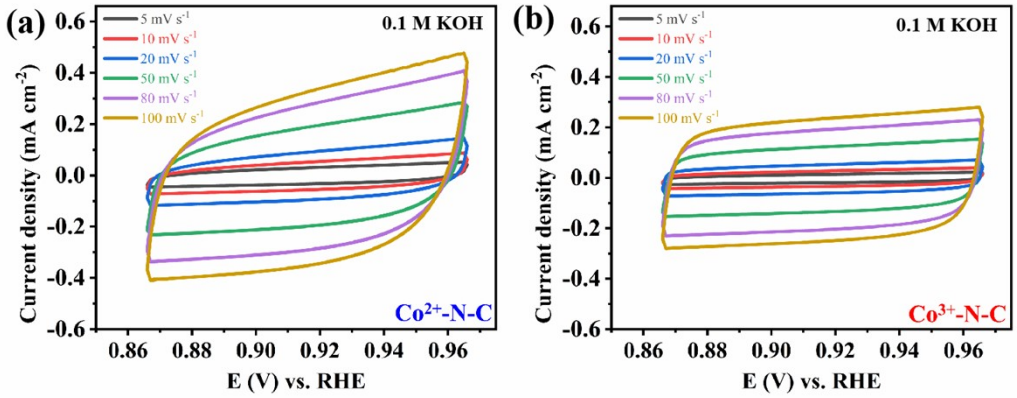

Figure S7. CV curves at different scan rates in 0.1 M KOH electrolyte solution: (a) **Co^{2+}−N−C**; (b) **Co^{3+}−N−C**.

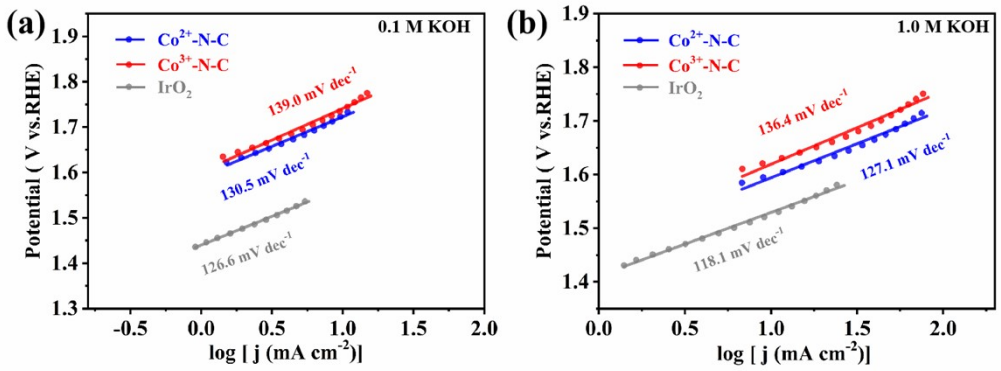

Figure S8. Comparison of Tafel slopes for **Co−N−C** catalysts with two different metal valence state centers and commercial IrO_2 catalyst in different electrolyte solutions: (a) 0.1 M KOH; (b) 1.0 M KOH.

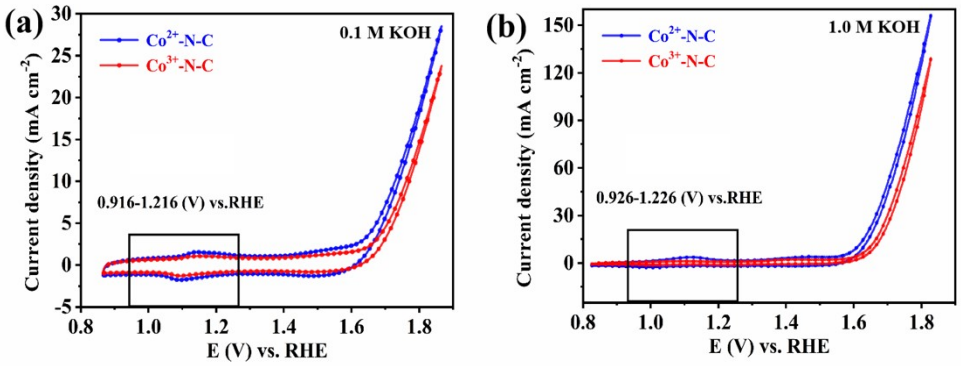

Figure S9. CV curves of **Co−N−C** catalysts with two different metal valence state centers in different electrolyte solutions: (a) 0.1 M KOH; (b) 1.0 M KOH.

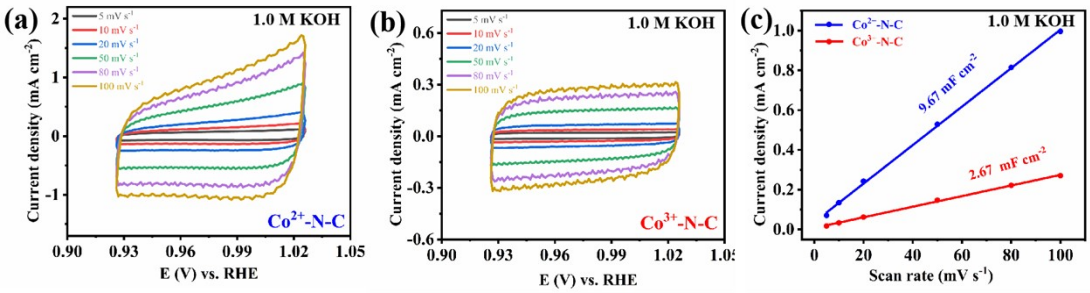

Figure S10. CV curves at different scan rates in 1.0 M KOH electrolyte solution: (a) CV scans of **Co^{2+}−N−C**; (b) CV scans of **Co^{3+}−N−C**; (c) Calculated electric double-layer capacitance (C_{dl}) slope.

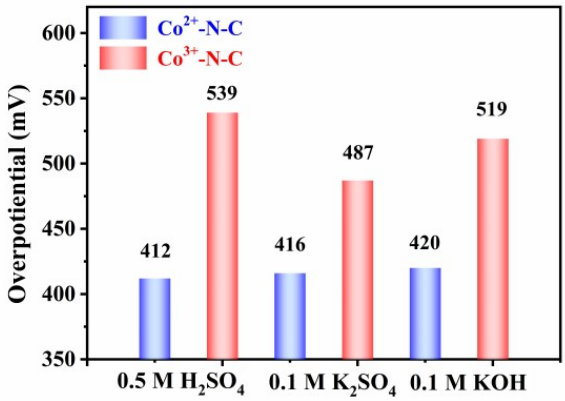

Figure S11. Comparison of overpotentials at a current density of 10 mA cm^{-2} for **Co−N−C** catalysts with two different metal valence state centers in 0.5 M H_2SO_4, 0.1 M K_2SO_4, and 0.1 M KOH electrolytes, based on HER performance testing LSV curves.

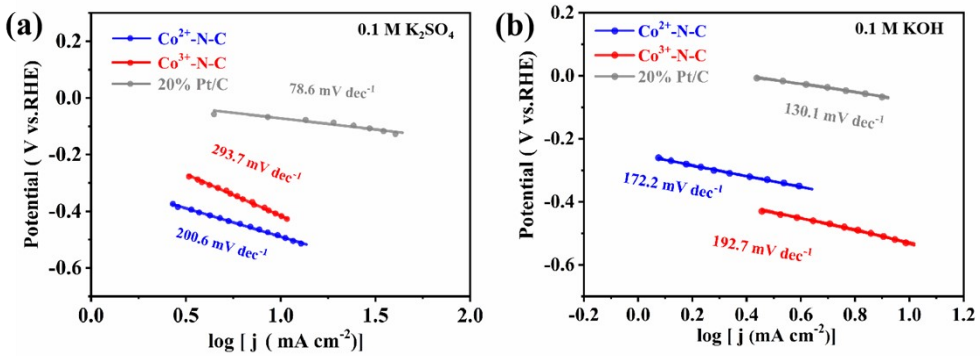

Figure S12. Comparison of Tafel slopes based on HER performance testing LSV curves for **Co−N−C** catalysts with two different metal valence state centers and commercial 20% Pt/C in different electrolytes: (a) 0.1 M K_2SO_4 electrolyte; (b) 0.1 M KOH electrolyte.

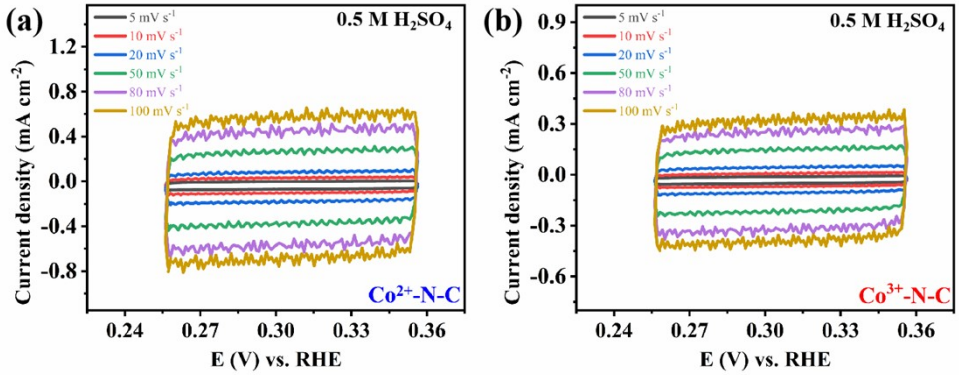

Figure S13. CV curves at different scan rates in 0.5 M H_2SO_4 electrolyte solution: (a) CV scans of **Co^{2+}−N−C**; (b) CV scans of **Co^{3+}−N−C**.

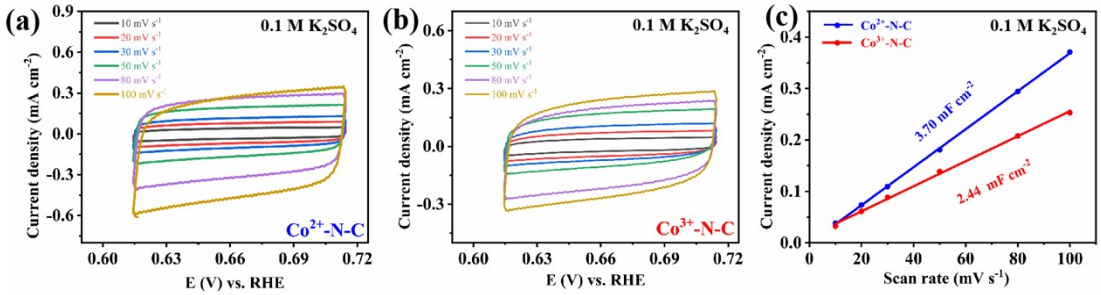

Figure S14. CV curves at different scan rates in 0.1 M K_2SO_4 electrolyte solution: (a) CV scans of **Co^{2+}–N–C**; (b) CV scans of **Co^{3+}–N–C**; (c) Calculated electric double-layer capacitance (C_{dl}) slope.

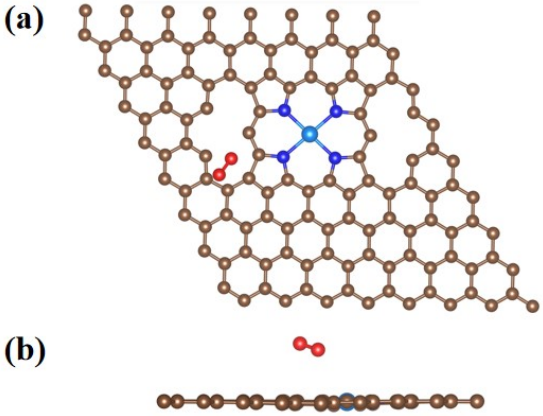

Figure S15. the Top and side view of O_2 adsorbed on the carbon vacancy site.

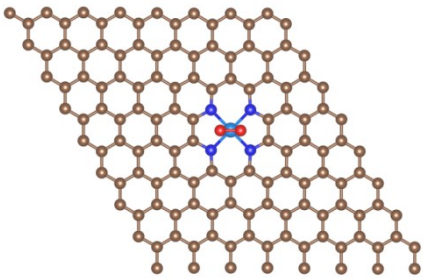

Figure S16. the optimized O_2 adsorbed on Co^{2+}–N–C by side-on configuration.

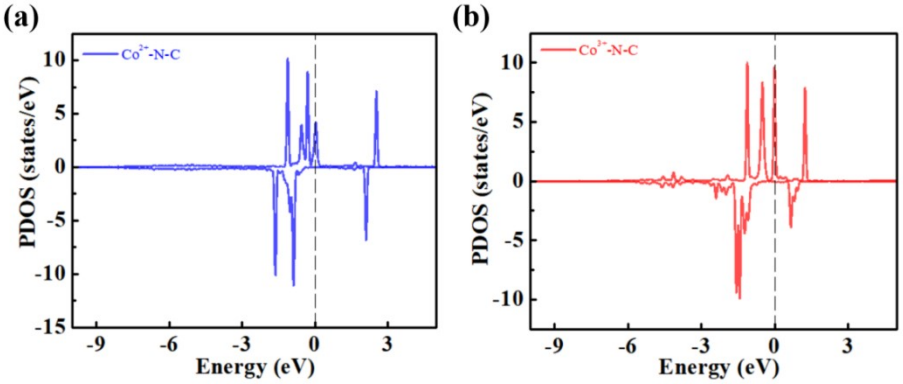

Figure S17. the partial density of states (PDOS) of (a) Co^{2+}–N–C and (b) Co^{3+}–N–C.

Table S1. Different types of C credit ratios.

Samples C types	C−C/Co−C	C=N	C−N	π−π*
Co^{2+}−N−C	56.77 %	30.09 %	6.15 %	6.99 %
Co^{3+}−N−C	65.34 %	21.71 %	5.68 %	7.27 %

Table S2. The proportion of N type integral surfaces.

Samples N types	Pyridinic-N	Pyrrolic-N	Graphitic-N	Oxidized-N
Co^{2+}−N−C	54.42 %	28.12 %	9.12 %	8.34 %
Co^{3+}−N−C	45.27 %	34.78 %	10.83 %	9.12 %

Table S3. Electrocatalytic performance (ORR) compared with similar catalysts.

Catalyst	Onsetpotentials (V)	Half-wave potentials (V)	Stability	Electrolyte
Co^{2+}−N−C[This work]	**0.86**	**0.77**	**252 h, 91.3%**	**0.1 M KOH**
CoNi−SAs/NC[12]	0.88	0.76	16 h, 90%	0.1 M KOH
Fe_1−HNC−500−850[13]	0.93	0.842	20000 s	0.1 M KOH
Co−SAs@NC[14]	0.96	0.82	22.5 h, 94.4%	0.1 M KOH
Co−CoN_4@NCNs[15]	0.95	0.83	12 h, 96.7%	0.1 M KOH
Co/Co−N−C[16]	0.86	0.78	–	0.1 M KOH
Co−N−C−850[17]	0.827	0.74	–	0.1 M KOH
Fe_3C@C−SN/25−800[18]	0.844	0.670	20000 s, ＞ 95.00%	0.1 M KOH
FeCo-DACs[19]	–	0.89	–	0.1 M KOH
FeCo-NCNS[20]	–	0.90	15 mV@10,000 cycles	0.1 M KOH
CoFeCu-TAC[21]	1.055	0.891	7 mV@10,000 cycles	0.1 M KOH
CoNi@NCNTs-LDH/CC [22]	-	0.84	16 h, 88.6%	0.1 M KOH

Table S4. Electrocatalytic performance (OER) compared with similar catalysts.

Catalyst	Current density	η (mV)	Electrolyte
Co^{2+}–N–C[This work]	10 mA cm^{-2}	**495**	**0.1 M KOH**
Co^{2+}–N–C[This work]	10 mA cm^{-2}	**368**	**1.0 M KOH**
Mn/Co−N−C−0.02−800[23]	10 mA cm^{-2}	430	0.1 M KOH
FeCo/Co−N−C[24]	10 mA cm^{-2}	380	0.1 M KOH
Co−N−C/rGO−6−600[25]	10 mA cm^{-2}	490	0.1 M KOH
CoNC−MOG−9[26]	10 mA cm^{-2}	400	0.1 M KOH
CoSA/NPC[27]	10 mA cm^{-2}	440	0.1 M KOH
CPN−C@900[28]	10 mA cm^{-2}	420	0.1 M KOH
Co−N−C/AC[29]	10 mA cm^{-2}	340	1.0 M KOH
P-doped-Co@NC3/1[30]	10 mA cm^{-2}	340	1.0 M KOH
CoP[31]	10 mA cm^{-2}	400	1.0M KOH
Ni_xCo_{1-x}@$Ni_xCo_{1-x}O$/NCNT[32]	10 mA cm^{-2}	380	1.0 M KOH
$NiCo(OH)_2$/NF[33]	10 mA cm^{-2}	420	1.0 M KOH
Co−P/Co−N−C/NPC[34]	10 mA cm^{-2}	374	1.0 M KOH
CoNi-PI(3,4-dihydroxyphthalimide)[35]	10 mA cm^{-2}	205	1.0 M KOH
F-doped $NiCo_2O_4$[36]	10 mA cm^{-2}	300	1.0 M KOH
CoNi-NBs[37]	10 mA cm^{-2}	300	1.0 M KOH

Table S5. Integral area and calculated capacitance data.

Electrolyte and Samples	0.1 M KOH **Co^{2+}–N–C**	0.1 M KOH **Co^{3+}–N–C**	1.0 M KOH **Co^{2+}–N–C**	1.0 M KOH **Co^{3+}–N–C**
Area (mA)	0.00387	0.00281	0.01630	0.00512
Q (mC)	0.000271	0.000197	0.001141	0.000358
Compared with 0.1 M KOH	1.38	1.00	7.16	1.82

Co^{3+}−N−C			

Table S6. Electrocatalytic performance (HER) compared with similar catalysts.

Catalyst	Current density	η (mV)	Electrolyte
Co^{2+}−N−C [This work]	**10 mA cm^{-2}**	**412**	**0.5 M H_2SO_4**
Co@N−CNTF[38]	10 mA cm^{-2}	226	0.5 M H_2SO_4
MoS_2 monolayer[39]	10 mA cm^{-2}	300	0.5 M H_2SO_4
N,P−graphene−1[40]	10 mA cm^{-2}	422	0.5 M H_2SO_4
CoNC/GD[41]	10 mA cm^{-2}	340	0.5 M H_2SO_4
Co_9S_8@MoS_2/CNFs[42]	10 mA cm^{-2}	190	0.5 M H_2SO_4
CNT/Co−PcC[43]	10 mA cm^{-2}	200	0.5 M H_2SO_4
4.55%Co−N/C[44]	10 mA cm^{-2}	263	0.5 M H_2SO_4

References：

1 Wu, W., Huang, L., Li, Y., Li, M., Chen, Y., Yang, Y., Chen, X., Wu, Y., Gu, L. and Cao, X., On-Site Production of Dilute H_2O_2 with Zinc-Air Battery, *Adv. Mater. Technol.*, 2022, **7**, 2100708.

2 Xu, H.; Zheng, D. J.; Wang, S.; Zheng, E. Y.; Zhang, Y.; Liu, T.; Liu, J.; Menga, D.; Kim, J.; Fang, J.-H.; Wang, X.; Zhang, Z.; Schrock, L.; Wang, J.; Lee, S.; Yu, S.; Iriawan, H.; Zhu, G.; Roman-Leshkov, Y.; Li, J.; Shao-Horn, Y. *J. Am. Chem. Soc*. 2025, **147**, 29838–29851.

3 Chen, Y.; Li, Q.; Lin, Y.; Liu, J.; Pan, J.; Hu, J.; Xu, X. Boosting Oxygen Evolution Reaction by FeNi Hydroxide-Organic Framework Electrocatalyst toward Alkaline Water Electrolyzer. *Nat. Commun*. 2024, **15**, 7278.

4 Sun, L. Z.; Pan, X.; Xie, Y. N.; Zheng, J. G.; Xu, S. H.; Li, L. N. Zhao, G. H. Accelerated Dynamic Reconstruction in Metal–Organic Frameworks with Ligand Defects for Selective Electrooxidation of Amines to Azos Coupling with Hydrogen Production. *Angew. Chem. Int. Ed*. 2024, **63**, e202402176.

5 Blöchl, P. E., Projector augmented-wave method, *Phys. Rev. B*, 1994, **50**, 17953-17979.

6 Hammer, B., Hansen, L. B. and Nørskov, J. K., Improved adsorption energetics within density-functional theory using revised Perdew-Burke-Ernzerhof functionals, *Phys. Rev. B*, 1999, **59**, 7413-7421.

7 Kresse, G. and Furthmüller, J., Efficiency of ab-initio total energy calculations for metals and semiconductors using a plane-wave basis set, *Comput. Mater. Sci.*, 1996, **6**, 15-50.

8 Perdew, J. P., Burke, K. and Ernzerhof, M., Generalized Gradient Approximation Made Simple, *Phys. Rev. Lett.*, 1996, **77**, 3865-3868.

9 Grimme, S., Semiempirical GGA-type density functional constructed with a long-range dispersion correction, *J. Comput. Chem.*, 2006, **27**, 1787-1799.

10 Kresse, G. and Furthmüller, J., Efficient iterative schemes for ab initio total-energy calculations using a plane-wave basis set, *Phys. Rev. B*, 1996, **54**, 11169-11186.

11 Hammer, B., Hansen, L. B. and Nørskov, J. K., Improved adsorption energetics within density-functional theory using revised Perdew-Burke-Ernzerhof functionals, *Phys. Rev. B*, 1999, **59**, 7413-7421.

12 Han, X., Ling, X., Yu, D., Atomically Dispersed Binary Co-Ni Sites in Nitrogen-Doped Hollow Carbon Nanocubes for Reversible Oxygen Reduction and Evolution, *Adv. Mater.*, 2019, **31**,

1905622.

13 Zhang, X., Zhang, S. and Yang, Y., A General Method for Transition Metal Single Atoms Anchored on Honeycomb-Like Nitrogen-Doped Carbon Nanosheets, *Adv. Mater*., 2020, **32**, 1906905.

14 Han, X., Ling, X., Wang, Y., Ma, T., Zhong, C., Hu, W. and Deng, Y., Generation of Nanoparticle, Atomic-Cluster, and Single-Atom Cobalt Catalysts from Zeolitic Imidazole Frameworks by Spatial Isolation and Their Use in Zinc-Air Batteries, *Angew. Chem. Int. Ed.*, 2019, **58**, 5359−5364.

15 Ding, K., Hu, J., Luo, J., Zhao, L., Jin, W., Liu, Y., Wu, Z., Zou, G., Hou, H. and Ji, X., Robust Electronic Correlation of Co-CoN4 Hybrid Active Sites for Durable Rechargeable Zn-Air Batteries, *Adv. Funct. Mater*., 2022, **32**, 2207331.

16 Yu, P., Wang, L., Sun, F., Xie, Y., Liu, X., Ma, J., Wang, X., Tian, C., Li, J. and Fu, H., Co Nanoislands Rooted on Co-N-C Nanosheets as Efficient Oxygen Electrocatalyst for Zn-Air Batteries, *Adv. Mater.*, 2019, **31**, 1901666.

17 Zhang, L., Yuan, J., Xu, Q., Zhang, F., Sun, Q. and Xie, H., Noble-metal-free Co-N-C catalyst derived from cellulose-based poly(ionic liquid)s for highly efficient oxygen reduction reaction, *Int. J. Biol. Macromol*., 2023, **242**, 125110.

18 Jaiswal, A., Kumar, R. and Prakash, R., Enhanced Electrocatalytic Oxygen Reduction Performance of Differently Optimized S, N Heteroatom Dual-Doped Carbon-Encapsulated Iron Carbide-Carbon (Fe3C@C-SN) Nanostructures, *ACS Appl. Energy Mater.*, 2023, **6**, 7803−7817.

19 Qiao J., You Y., Kong L., Feng W., Zhang H., Huang H., Li C., He W. and Sun Z. M., Precisely Constructing Orbital-Coupled Fe–Co Dual-atom Sites for High-Energy-Efficiency Zn–Air/Iodide Hybrid Batteries, *Adv. Mater.*, 2024, **36**, 2405533.

20 Tang X., Zhang Y., Tang S., Lützenkirchen-Hecht D., Yuan K. and Chen Y., Structural and Chemical Origin of Dual-Atom Sites for Enhanced Oxygen Electroreduction, *ACS Catal.*, 2024, **14**, 13065–13080.

21 Zhong J. J., Liang Z. H., Liu N., Xiang Y. C., Yan B., Zhu F. Y., Xie X., Gui X. C., Gan L. Y., Yang H. B., Yu D. S., Zeng Z. P. and Yang G. W., Engineering Symmetry-Breaking Centers and d-Orbital Modulation in Triatomic Catalysts for Zinc-Air Batteries, *ACS Nano*, 2024, **18**, 5258 − 5269.

22 Tian W. W., Ren J. T., Wang H. Y., Wang L. and Yuan Z. Y., Bioinspired binary-site catalysts for novel urea-assisted Zn-air battery: A transfer station between renewable energy and hydrogen, *Applied Catalysis B: Environment and Energy*, 2024, **354**, 124115.

23 Wei, L. C., Qiu, L. J., Liu, Y. Y., Zhang, J. M., Yuan, D. S. and Wang, L., Mn-doped Co-N-C dodecahedron as a bifunctional electrocatalyst for highly efficient Zn-air batteries, *ACS Sustainable Chem. Eng*., 2019, **7**, 14180−14188.

24 Zhong, J., Zhu, Z., Xu, Q., Peng, L., Luo, K. and Yuan, D., FeCo Alloy Nanoparticles Supported on Co-N-C Cubes Derived from Imidazolate Frameworks as a Bifunctional Electrocatalyst for Rechargeable Zinc-Air Batteries, *Energy Fuels*, 2023, **37**, 13489–13497.

25 Cai, S., Wang, R., Yourey, W. M., Li, J., Zhang, H. and Tang, H., An efficient bifunctional electrocatalyst derived from layer-by-layer self-assembly of a three-dimensional porous Co-N-C@graphene, *Sci. Bull*., 2019, **64**, 968–975.

26 Shang, N., Li, S., Zhou, X., Gao, S., Gao, Y., Wang, C., Wu, Q. and Wang, Z., Co/nitrogen-doped carbon nanocomposite derived from self-assembled metallogels as efficient bifunctional oxygen electrocatalyst for Zn-air batteries, *Appl. Surf. Sci*., 2021, **537**, 147818.

27 Liu, X., Zhang, Y., Zhao, Z., Gao, H., Kang, J., Wang, R., Ge, G. and Jia, X., Highly exposed discrete Co atoms anchored in ultrathin porous N, P-codoped carbon nanosheets for efficient oxygen electrocatalysis and rechargeable aqueous/solid-state Zn-air batteries, *J. Mater. Chem. A*, 2021, **9**, 22643–22652.

28 Yu, J., Chen, Z. and Zhong, L., Bamboo fiber-derived bifunctional electrocatalyst for rechargeable Zn-air batteries, *Ionics*, 2023, **29**, 3193–3202.

29 Li, X., Lv, X., Sun, P. and Sun, X., Synergistic Pore Structure and Active Site Modulation in Co-N-C Catalysts Enabling Stable Zinc-Air Batteries, *ACS Appl. Mater. Interfaces*, 2024, **16**, 29979–29990.

30 Li, Y.-L., Jia, B., Fan, Y., Zhu, K., Li, G. and Su, C.-Y., Bimetallic Zeolitic Imidazolite Framework Derived Carbon Nanotubes Embedded with Co Nanoparticles for Efficient Bifunctional Oxygen Electrocatalyst, *Adv. Energy Mater.*, 2018, **8**, 1702048.

31 Sumit, Borah, A., Palaniyappan, S. and Rajeshkhanna, G., ZIF-67-derived Co-N-C supported nickel cobalt sulfide as a bifunctional electrocatalyst for sustainable hydrogen production via alkaline electrolysis, *Nanoscale*, 2024, **16**, 14020–14032.

32 Behera, S., Chauhan, C. and Mondal, B., Co-N-C/C Bifunctional Electrocatalyst for Dual Applications in Seawater Electrolysis and Catalyst in Hydrazine Fuel Cells, *Small*, 2024, **20**, 2311946.

33 Sung, M. C., Lee, G. H. and Kim, D. W., $CeO_2/Co(OH)_2$ hybrid electrocatalysts for efficient hydrogen and oxygen evolution reaction, *J. Alloys Compd.*, 2019, **800**, 450–455.

34 Lv, X., Xiao, Z., Wang, H., Wang, X., Shan, L., Wang, F. and Chen, Y., In situ construction of Co/N/C-based heterojunction on biomass-derived hierarchical porous carbon with stable active sites using a Co-N protective strategy for high-efficiency ORR, OER and HER trifunctional electrocatalysts, *J. Energy Chem.*, 2021, **54**, 626–638.

35 Y. Weng, L. Sun, H. Jia, W. Shang, J. J. Chen, B. Dhara, Y. Chen, F. Huang, S. Han, H. He, B. Yin, Homonuclear/Heteronuclear Bimetallic Conjugated Coordination Polymers with Customized Oxygen Evolution Pathway, *J. Am. Chem. Soc.*, 2025, **147**, 13928.

36 Yue Y., Zhong X. Y., Sun M. Z., Du J., Gao W. S., Hu W., Zhao C. Y., Li J., Huang B. L., Li Z. L. and Li C., Fluorine Engineering Induces Phase Transformation in $NiCo_2O_4$ for Enhanced Active Motifs Formation in Oxygen Evolution Reaction, *Adv. Mater.*, 2025, **37**, 2418058.

37 Y. Zhao, N. Dongfang, C. Huang, R. Erni, J. Li, H. Zhao, L. Pan, G. R. Patzke, Operando monitoring of the functional role of tetrahedral cobalt centers for the oxygen evolution reaction，*Nat. Commun.* 2025, **16**, 580.

38 Guo, H. L., Feng, Q. C., Zhu, J. X., Xu, J. S., Li, Q. Q., Liu, S. L., Xu, K. W., Zhang, C. and Liu, T. X., Cobalt nanoparticle-embedded nitrogen-doped carbon/carbon nanotube frameworks derived from a metal-organic framework for tri-functional ORR, OER and HER electrocatalysis, *J. Mater. Chem. A*, 2019, **7**, 3664–3672.

39 Zhang, J., Wu, J., Guo, H., Chen, W., Yuan, J., Martinez, U., Gupta, G., Mohite, A., Ajayan, P. M. and Lou, J., Unveiling Active Sites for the Hydrogen Evolution Reaction on Monolayer MoS_2, *Adv. Mater.*, 2017, **29**, 1701955.

40 Zheng, Y., Jiao, Y., Li, L. H., Xing, T., Chen, Y., Jaroniec, M. and Qiao, S. Z., Toward design of synergistically active carbon-based catalysts for electrocatalytic hydrogen evolution, *ACS Nano*, 2014, **8**, 5290–5296.

41 Xue, Y., Li, J., Xue, Z., Li, Y., Liu, H., Li, D., Yang, W. and Li, Y., Extraordinarily Durable Graphdiyne-Supported Electrocatalyst with High Activity for Hydrogen Production at All Values

of pH, *ACS Appl. Mater. Interfaces*, 2016, **8**, 31083–31091.

42 Zhu, H., Zhang, J., Yanzhang, R., Du, M., Wang, Q., Gao, G., Wu, J., Wu, G., Zhang, M., Liu, B., Yao, J. and Zhang, X., When cubic cobalt sulfide meets layered molybdenum disulfide: a core-shell system toward synergetic electrocatalytic water splitting, *Adv. Mater.*, 2015, **27**, 4752–4759.

43 Sa, Y. J., Park, S. O., Jung, G. Y., Shin, T. J., Jeong, H. Y., Kwak, S. K., Joo, S. H. and Hoon, S., Heterogeneous Co-N/C Electrocatalysts with Controlled Cobalt Site Densities for the Hydrogen Evolution Reaction: Structure-Activity Correlations and Kinetic Insights, *ACS Catal.*, 2019, **9**, 83−97.

44 Du, Y., Chen, H., Huang, Z., He, X., Fang, W., Li, W. and Zhao, L., Unique size of Co nanoparticles encapsulated in N-rich carbon structure derived from electrochemical etching for enhanced electrocatalytic hydrogen evolution, ACS Appl. *Energy Mater.*, 2020, **3**, 687−694.